A 75 - 170 GHz Active Mixer based on Time-Varying Transconductance Modulated by a Passive Current-Domain LO Feed in 22 nm FDSOI

Sarah Koop-Brinkmann#, Victor Lasserre#, Andrea Mazzanti$, Vadim Issakov#
#Institute for CMOS Design, Technische Universität Braunschweig, Germany
$Department of Electrical, Computer and Biomedical Engineering, University of Pavia, Italy
s.koop-brinkmann@tu-braunschweig.de

***Abstract*— This work presents an ultra-wideband active nonlinearity-based CMOS mixer operating up to 170 GHz. The transconductance of a differential pair is modulated by varying the tail current $\mathbf{I_{tail}}$ with a periodicity of the input local oscillator (LO) signal $T_{\mathrm{LO}} = 1/f_{\mathrm{LO}}$. LO input voltage is converted into current by a wideband passive network, which also provides a passive transconductance gain. Feeding LO in the current domain enables an extremely wideband operation. Additional advantages of the proposed mixer topology are: a) no need for high LO power levels; b) LO is in common-mode and RF in differential, providing good LO-RF isolation; c) high conversion gain at low DC power consumption. The circuit is realized in 22 nm FDSOI CMOS and dissipates only 2.2 mW from a single 0.8 V supply, including an IF buffer. The mixer shows a measured voltage conversion gain of 15 dB and an exceptional 3-dB bandwidth of 75-170 GHz.**

I. Introduction

There is a growing interest in wideband millimeter-wave building blocks for integrated on-chip vector network analyzers (VNA) [1]. This is driven by the demand for miniaturization and cost effective in-situ device-under-test characterization, e.g. for permittivity based analysis and spectroscopy in portable point-of-care biomedical applications [1], demanding low P_{DC}. One of the key components in a VNA front-end is a mixer. A frequency range from 75 GHz up to 170 GHz is of high interest, since it extends measurement capabilities of existing portable VNAs and enables omitting bulky external W-band (75-110 GHz) and D-band (110-170 GHz) extenders.

Design of ultra-wideband mm-wave components covering more than octave of bandwidth is challenging and typically requires e.g. synthesis of complex high-order multi-resonant matching networks [2], use of doubly-tuned transformers, staggered tuned stages or distributed structures.

In this work we show an ultra-wideband down-conversion active mixer using time-varying transconductance. The circuit utilizes high-order passive network at the LO port, which converts the LO voltage into current, as shown in Fig. 1(b). Unlike the Gilbert-cell mixer, the time varying $\mathrm{G_m}(t)$ solution does not require current switching by a large LO voltage amplitude and allows omitting the LO switching pair, as shown in Fig. 1. The proposed ciruit is an *additive* nonlinearity-based mixer, while Gilbert-cell is a *multiplication*-based mixer. Another approach that proposes swapping the RF and LO ports is the switched tranconductance mixer [3], [4]. However, it achieved only 10 GHz, since it operates in voltage domain and requires turning transistors fully off. In our work, transistors are not hard switched and the circuit works up to 170 GHz.

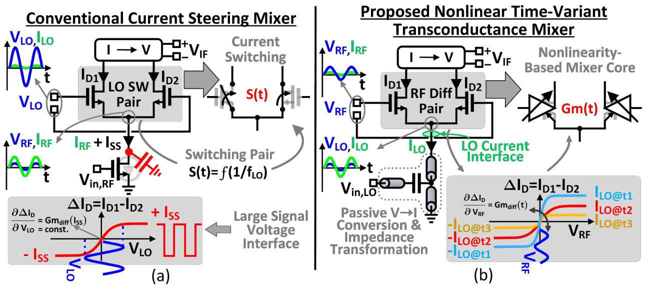

Fig. 1. Conceptual block diagrams of (a) classical Gilbert-cell mixer and (b) the proposed nonlinearity-based time-variant transconductance mixer.

II. Mixer Operating Principle and Circuit Design

The schematic of the proposed wideband mixer including an intermediate frequency (IF) buffer is shown in Fig. 2. The active mixer core uses a capacitively neutralized differential pair (M1). The RF signal $v_{\mathrm{RF,in}}(t) = V_{\mathrm{RF}}\cos(\omega_{\mathrm{RF}}t)$ is applied differentially to the gates through the balun T1. The LO input signal $v_{\mathrm{LO,in}}(t) = V_{\mathrm{LO,in}}\cos(\omega_{\mathrm{LO}}t)$ is converted to current $i_{\mathrm{LO}}(t) = g_{\mathrm{m,LO}} \cdot v_{\mathrm{LO,in}}(t)$ using a *passive* g_{m} network ($g_{\mathrm{m,LO}}$) comprised of transmission lines TL1-TL5 and capacitors C2-C3. $i_{\mathrm{LO}}(t)$ is fed in common-mode at source node P. First, we analyze the nonlinear mixer core. The simplified EKV (sEKV) model is used to accurately describe the circuit analytically across all operation regions. The drain current of differential-pair transistors M1 is given by [5]

$$I_{\mathrm{D,M1}} = \frac{I_{\mathrm{spec}} \cdot 4\left(q_{\mathrm{s}}^2 + q_{\mathrm{s}}\right)}{2 + \lambda_c + \sqrt{4\left(1+\lambda_c\right) + \lambda_c^2(1+2q_{\mathrm{s}})^2}}, \tag{1}$$

with the specific current $I_{\mathrm{spec}} = I_{\mathrm{spec}\square} \cdot W/L$, the velocity saturation parameter λ_c and the normalized inversion charge at the source q_{s}. For small overdrive voltages V_{ov}, i.e., M1 is biased in weak or moderate inversion, Eq. 1 can be further simplified by neglecting the square term of q_{s} in the root. Thus,

$$I_{\mathrm{D,M1}} \approx \frac{W}{L} \cdot \frac{I_{\mathrm{spec}\square} \cdot 4\left(q_{\mathrm{s}}^2 + q_{\mathrm{s}}\right)}{2 + \lambda_c + \sqrt{4\left(1+\lambda_c\right)}} = \alpha \cdot \left(q_{\mathrm{s}}^2 + q_{\mathrm{s}}\right), \tag{2}$$

describes $I_{\mathrm{D,M1}}$ as a function of the inversion charge q_{s}, scaled with the technology-dependent constant α. To relate $I_{\mathrm{D,M1}}$ to LO and RF inputs, applied at gate and source, q_{s} must be related to V_{ov}. Using the Wright omega function, one obtains

$$q_{\mathrm{s}} = \frac{1}{2} w \left(\ln(2) + \frac{V_{\mathrm{ov}}}{n\,U_{\mathrm{T}}}\right), \tag{3}$$

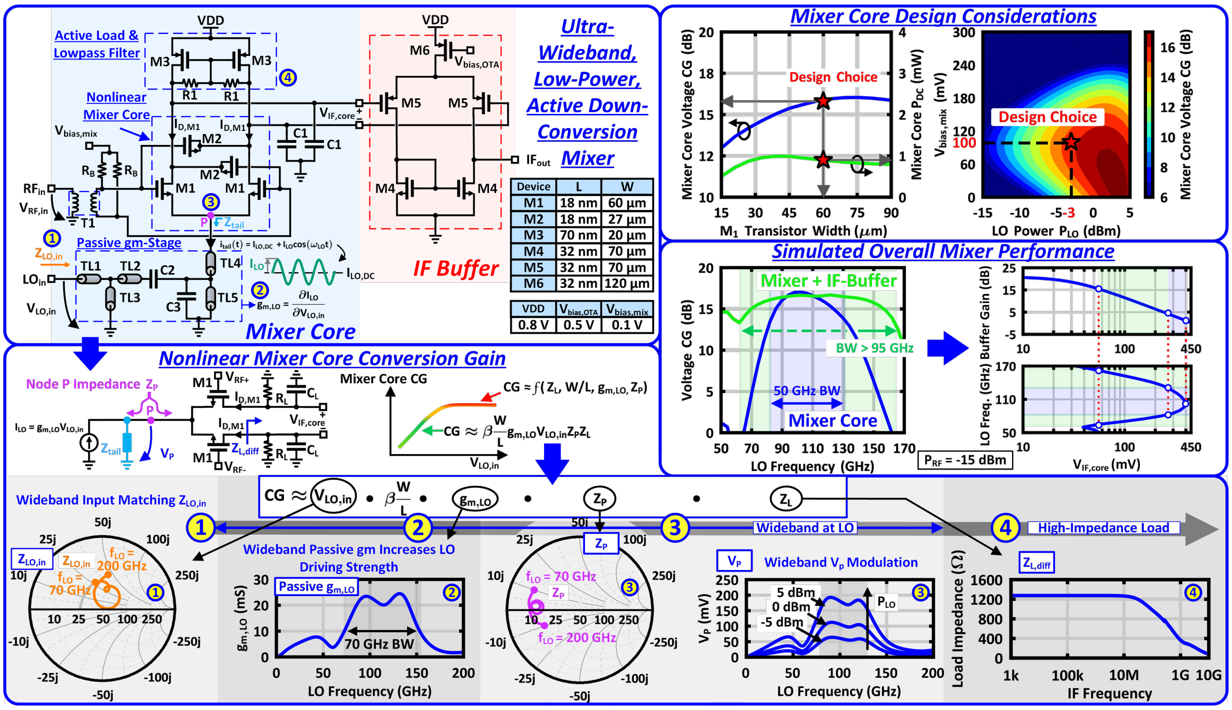

Fig. 2. Schematic of the proposed ultra-wideband, low-power active down-conversion mixer (top left); simplified nonlinear mixer core half-circuit (center left); mixer core design considerations (top right); simulated overall mixer performance (center right); and frequency characteristics along the signal chain (bottom).

Table 1. Extracted sEKV Parameters for M1 (W=60 µm/L=18 nm).

n	I_{spec}	V_{T0}	λ_c	σ_d	$V_T \approx V_{T0}(1-\sigma_d V_{DS})$
1.51	2.46 mA	164 mV	0.412	0.0522	161 mV | V_{DS} = 350 mV

where $U_T = kT/q$, n is slope factor [5] and $V_{ov} = V_{GS} - V_T$. The extracted sEKV coefficients for M1 are given in Tab. 1. For further derivations, Eq. 3 can be described by a Taylor series expansion of the Wright omega function around $V_{ov} = 0\,$V. Considering terms up to the 4th order yields

$$q_s \approx a + \frac{b}{n\,U_T}V_{ov} + \frac{c}{(n\,U_T)^2}V_{ov}^2 + \frac{d}{(n\,U_T)^3}V_{ov}^3 + \frac{e}{(n\,U_T)^4}V_{ov}^4, \tag{4}$$

where a-e are Taylor coefficients, given in Tab. 2. Finally, by plugging q_s (Eq. 4) into Eq. 1, the drain current $I_{D,M1}$ can be expressed as a function of V_{ov} with series expansion coefficients c'_k, summarized in Tab. 2, as follows

$$I_{D,M1} = \alpha \cdot \sum_{k=0}^{K} c'_k \cdot \left(\frac{V_{ov}}{n\,U_T}\right)^k. \tag{5}$$

Referring to schematic in Fig. 2, $I_{D,M1}$ can be described as a function of the LO and RF inputs, by expressing V_{ov} as

$$\begin{aligned} V_{ov} &= V_{GS} - V_T = [v_{RF}(t) + V_{bias,mix} - v_P(t)] - V_T \\ &= V_{DC} + V_{RF}\cos(\omega_{RF}t) - Z_P\,I_{LO}\cos(\omega_{LO}t)\,, \end{aligned} \tag{6}$$

where Z_P and I_{LO} are impedance and LO current at the common-source node P in Fig. 2, yielding voltage amplitude $V_P = Z_P I_{LO}$ at this node. V_{ov} in Eq. 6 has a DC component $V_{DC} = V_{bias,mix} - V_T$ and two AC components at ω_{RF} and ω_{LO}. Combining Eqs. 5 and 6, we see that this is an *additive* mixer, since a sum goes thru nonlinearity and yields a harmonic-rich current $I_{D,M1}$. Terms for $k \geq 2$ result in $\cos(\omega_{RF}t) \cdot \cos(\omega_{LO}t)$, yielding the wanted $\omega_{IF} = \omega_{RF} - \omega_{LO}$ component after a low-pass filter. Considering only IF components of the current and converting into an output voltage thru Z_L, presented by the active load in Fig. 2, we obtain the voltage conversion gain, defined as $\mathrm{CG} = \frac{V_{IF}|_{\omega=\omega_{RF}-\omega_{LO}}}{V_{RF}|_{\omega=\omega_{RF}}}$, as function of bias, IF load, V_P, RF input amplitude and coefficients in Tab. 2. Accuracy of Eq. 7 is verified by comparing with simulation in Fig. 3.

$$\mathrm{CG} = \frac{\alpha Z_L V_P}{(n\,U_T)^2}\left[c'_2 + \frac{3c'_3 V_{DC}}{n\,U_T} + \frac{3c'_4(V_P^2 + V_{RF}^2 + 4V_{DC}^2)}{2(n\,U_T)^2}\right] \tag{7}$$

A very good analytical to simulation correlation is obtained

Table 2. Coefficients a-e (top) and resulting coefficients c'_k (bottom).

Coeff.	a	b	c	d	e
Value	$\omega_a/2$	$\frac{\omega_a}{2(1+\omega_a)}$	$\frac{\omega_a}{4(1+\omega_a)^3}$	$\frac{\omega_a(1-2\omega_a)}{12(1+\omega_a)^5}$	$\frac{\omega_a(6\omega_a^2-8\omega_a+1)}{48(1+\omega_a)^7}$

Coeff.	Value	Coeff.	Value
$c'_0 > 0$	$a^2 + a$	$c'_5 < 0$	$2be + 2cd$
$c'_1 > 0$	$2ab + b$	$c'_6 < 0$	$2ce + d^2$
$c'_2 > 0$	$b^2 + 2ac + c$	$c'_7 > 0$	$2de$
$c'_3 > 0$	$2bc + 2ad + d$	$c'_8 > 0$	e^2
$c'_4 < 0$	$2ae + 2bd + c^2 + e$	with $\omega_a = \omega(\ln(2))$	

already for $k \geq 4$, i.e. summing three terms in the series.

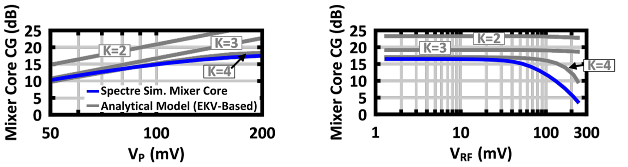

Fig. 3. Comparison of the EKV-based analytical model with Spectre simulations for M1, assuming $Z_{\mathrm{L,diff}} = 1200\Omega$.

Coefficient c_4' is negative (see Tab. 2) and causes thereby gain compression for sufficiently large LO input amplitude $V_{\mathrm{LO,in}}$ modulating $V_P = Z_P \cdot g_{\mathrm{m,LO}} \cdot V_{\mathrm{LO,in}}$. Therefore, it can be shown from Eq. 7 that CG is optimal for $V_{\mathrm{DC}} \approx 0\,\mathrm{V}$, which means biasing gate of M1 around V_{T}. However, the optimal gate bias point moves below V_{T} for larger $V_{\mathrm{LO,in}}$, as shown in the heatmap in Fig. 2. $V_{\mathrm{bias,mix}} < V_{\mathrm{T}}$ yields a negative V_{DC}, which boosts the gain thanks to negative c_5'. Consequently, the operation point below V_{T} places M1 in weak inversion and enhances gain by a stronger $I_{\mathrm{D,M1}}$ nonlinearity. This is also good for low DC power. CG scales with width of M1 thru coefficient α, defined in Eq. 2. The optimal width of 60 µm is chosen for high gain and low P_{DC}, as shown in Fig. 2. Next, to gain further insight, we consider only the first component in Eq. 7, which reduces to the following form

$$\mathrm{CG} \approx \frac{\alpha c_2'}{(n\,U_{\mathrm{T}})^2} I_{\mathrm{LO}} Z_{\mathrm{P}} Z_{\mathrm{L}} = \beta \frac{W}{L} g_{\mathrm{m,LO}} V_{\mathrm{LO,in}} Z_{\mathrm{P}} Z_{\mathrm{L}}, \qquad (8)$$

where β is a technology and bias dependent constant, obtained from Eqs. 2 and 8. Obviously, Eq. 2 is valid for small $V_{\mathrm{LO,in}}$ amplitudes. Yet, it visualizes the reason for *wideband* operation, as shown at the bottom of Fig. 2. First, the passive network at LO port offers wideband input matching. It also offers high $g_{\mathrm{m,LO}}$ over a bandwidth of 70 GHz. Next, the impedance Z_P at node P is wideband and around 10 Ω. This guarantees a current interface, moderate voltage swing V_P and avoiding hard switching. The voltage amplitude V_P scales with LO input power and remains constant over a wide frequency range. $Z_{\mathrm{L,diff}}$ realized by M3 offers a high load of 1.2 kΩ and low-pass filter functionality.

To gain even more insight, we take a derivative of the current in Eq. 5 with respect to the gate voltage to obtain time-varying transconductance G_{m}, modulated by the LO input

$$G_{\mathrm{m,M1}} = \frac{\partial I_{\mathrm{D,M1}}}{\partial V_{\mathrm{G}}} = \alpha \cdot \sum_{k=0}^{K} c_k' \cdot k \cdot \left(\frac{V_{\mathrm{ov}}}{n\,U_{\mathrm{T}}}\right)^{k-1}. \qquad (9)$$

In first approximation, as confirmed by simulation in Fig. 4, it is sufficient to consider only the DC and the first harmonic terms in the expansion of $G_{\mathrm{m,M1}} = G_{\mathrm{m,DC}} + G_{\mathrm{m,H1}}\cos(\omega_{\mathrm{LO}} t)$

$$G_{\mathrm{m,M1}} = \frac{\alpha}{nU_{\mathrm{T}}}\left[c_1' + \frac{2c_2' V_{\mathrm{P}}}{nU_{\mathrm{T}}}\cos(\omega_{\mathrm{LO}} t)\right]. \qquad (10)$$

First, it shows that by modulating the current at the source, G_m varies as sinusoidal function with periodicity $T_{\mathrm{LO}} = 1/f_{\mathrm{LO}}$. Second, RF voltage at the gate of M1 is converted into current thru $G_{\mathrm{m,M1}}$ and then to IF voltage thru Z_L, resulting in v_{IF} of the form $v_{\mathrm{IF}} = V_{\mathrm{RF}}\cos(\omega_{\mathrm{RF}} t)\left[G_{\mathrm{m,DC}} + G_{\mathrm{m,H1}}\cos(\omega_{\mathrm{LO}} t)\right] Z_L$. It results in CG $\approx \frac{1}{2} G_{\mathrm{m,H1}} \cdot Z_L = \left[\beta \frac{W}{L} g_{\mathrm{m,LO}} V_{\mathrm{LO,in}} Z_{\mathrm{P}}\right] Z_L$. This expression is similar to CG $\approx 2/\pi \cdot g_{\mathrm{m,RF}} \cdot Z_L$ for a Gilbert mixer. CG of Gilbert mixer can be increased by a higher current, hence P_{DC} thru $g_{\mathrm{m,RF}}$, while in this mixer gain can be achieved by a passive $g_{\mathrm{m,LO}}$, giving high gain efficiency.

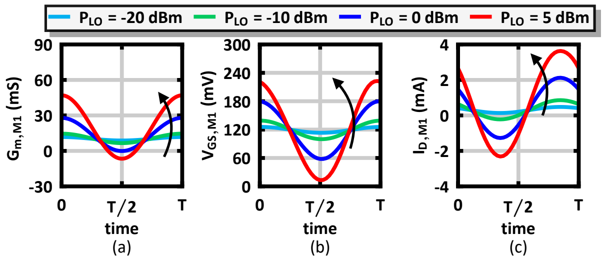

Fig. 4. Simulated impact of the LO drive power $\mathrm{P_{LO}}$ on the (a) $G_{\mathrm{m,M1}}$, (b) $\mathrm{V_{GS}}$ and (c) $\mathrm{I_D}$ waveforms of single transistor M_1 at f_{LO} = 100 GHz.

Another bandwidth enhancing effect is shown Fig. 2. It is related to the IF buffer. At frequency range in which $g_{\mathrm{m,LO}}$ is high, mixer core has a high gain. Large swing drives IF buffer into compression, reducing gain. Outside this range, when mixer core gain drops, IF swing into buffer lowers and its gain increases, compensating mixer gain (Fig.2, center, right).

The proposed topology has many advantages, but also a drawback, which is related to the 1/f noise. As shown in Fig. 5, the 1/f voltage source is present at the gate of M1 and appears at the IF output without frequency conversion. M1 acts as a CS stage without degeneration, since Z_P is low. Higher Z_P would reduce NF and enhance CG, but at cost of lower bandwidth. The overall NF is dominated by the noise of the mixer core.

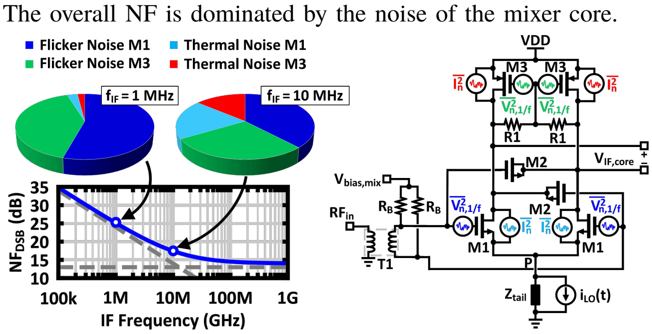

Fig. 5. Mixer core noise (a) simulation and contributors; (b) sources.

III. Measurement Results

The proposed mixer is fabricated in 22 nm FDSOI CMOS. The chip photo is shown in Fig. 6. The die is wire-bonded to a PCB to provide bias voltages, as well as a 0.8 V supply. As shown in Fig. 6, the RF and LO inputs are generated by Keysight 67 GHz signal generators and upconverted using frequency extension modules, a ×3/×6 frequency multiplier and Keysight W-/D-band extender. Additional attenuators are used to precisely adjust the input power levels, measured using R&S FSW85 spectrum analyzer with FS-Z110/-Z170 harmonic mixers. For conversion gain measurements in Fig. 7,

Table 3. Performance summary and comparison with state-of-the-art mm-wave mixers.

Reference	This work	RFIC 2024 [6]	RFIC 2023 [7]	TMTT 2024 [8]	MWTL 2023 [9]
Technology	**22 nm FDSOI CMOS**	28 nm bulk CMOS	40 nm CMOS	130 nm SiGe BiCMOS	28 nm bulk CMOS
Architecture	**Mixer + IF-Amp.**	IQ-SHM + LO-Buffer	N-Path Mixer + LO Buffer + IF-Amp.	IQ Active Mixer + IF-Amp.	Active Mixer + LO Buffer
Mixer Topology	**Nonlinearity-Based Gm_{diff} Modulation**	IQ Passive Subharmonic	$\lambda/4$ TL-matched N-Path Mixer	Gilbert Cell	Gilbert Cell
Relative Bandwidth (%)	**> 77.55**	14.35	7.06	27.59	14.29
RF Frequency (GHz)	**< 75 - 170**	110 - 127	82 - 88	125 - 165	130 - 150
IF Frequency	**100 kHz - 10 MHz**	100 kHz - 1 MHz	250 kHz - 10 MHz	1 GHz	11 GHz - 15 GHz
$P_{LO,in}$ (dBm)	**-10[1] / -3[2]**	-1	N.A.	1.9	-7
Voltage CG (dB)	**15**	-8.6	20	12.7	4.4
NF (dB)	**20**	15.7	9.5	8.2	8.3
P_{DC} (mW)	**2.2[3] / 1**	39.6	37	34	64
IP_{1dB} (dBm)	**-23[1] / -9[2]**	5	-5.2	-3.5	-7.4
Active Area (mm^2)	**0.02**	0.69	0.42	0.23	0.3

[1]measured with IF-Buffer, [2]simulated without IF-Buffer, [3]including IF-Buffer

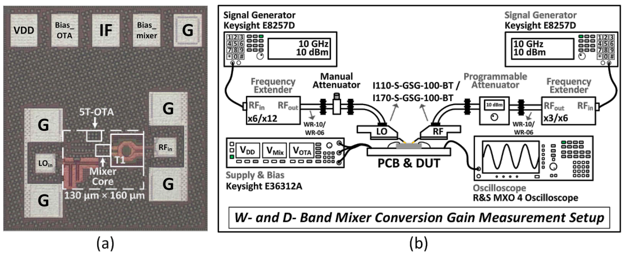

Fig. 6. (a) Chip microphotograph, and (b) W- and D-band setup.

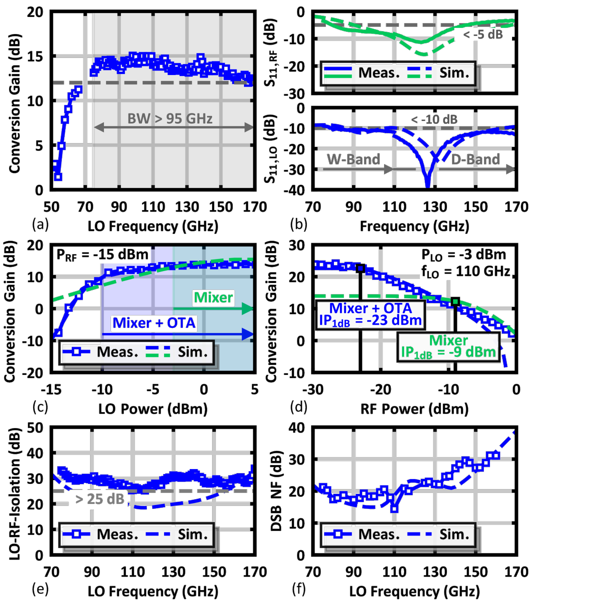

Fig. 7. Measured and simulated (a) CG versus RF frequency, (b) RF and LO input matching, CG versus (c) LO power and (d) RF power for f_{LO}=110 GHz, (e) LO-RF-isolation, and (f) DSB NF for f_{IF}=10 MHz.

the IF output is sensed with a high-impedance oscilloscope at an IF frequency of 1 MHz and the LO attenuator settings were chosen to ensure P_{LO} > -10 dBm over the respective frequency band. While consuming only 2.2 mW (including IF buffer), a high maximum voltage conversion gain (CG) of 15 dB is achieved, with an exceptional measured 3-dB bandwidth of 95 GHz ranging from 75 GHz to 170 GHz. The S_{11} is <-10 dB at the LO port and <-5 dB at the RF port almost over the entire frequency range of interest 75-170 GHz, as shown in Fig. 7(b). As shown in Fig. 7 (c), the mixer requires a low LO power of -3 dBm. Already -10 dBm is sufficient for the overall CG to saturate. Unfortunately, the IF buffer limits the measured RF linearity, yielding an IP_{1dB} of -23 dBm. The mixer alone achieves in simulation an IP_{1dB} of -9 dBm with a CG of 15 dB. A good LO-RF-isolation > 25 dB is measured over the 95 GHz 3dB operation bandwidth. LO-IF and RF-IF isolations could not be measured due to high suppression by the IF buffer. Fig. 7 (f) shows a DSB NF at IF of 10 MHz.

References

[1] I. Nasr *et al.*, "Single- and Dual-Port 50-100-GHz Integrated Vector Network Analyzers With On-Chip Dielectric Sensors," *IEEE TMTT*, vol. 62, no. 9, pp. 2168–2179, 2014.

[2] G. D. Filippi *et al.*, "A D-Band LNA Exploiting Ultra Wideband Sixth Order Matching Networks in SiGe BiCMOS," in *ESSERC*, 2024.

[3] E. Klumperink *et al.*, "A CMOS switched transconductor mixer," *IEEE JSSC*, vol. 39, no. 8, pp. 1231–1240, 2004.

[4] H. Li *et al.*, "A Low-Power Low-Noise Decade-Bandwidth Switched Transconductor Mixer With AC-Coupled LO Buffers," *IEEE TCAS-I: Regular Papers*, vol. 65, no. 2, pp. 510–521, 2018.

[5] C. Enz *et al.*, *Charge–Based MOS Transistor Modeling: The EKV model for low-power and RF IC design*. Wiley, 2006.

[6] S. Koop-Brinkmann *et al.*, "A Low Conversion Loss 120 GHz Passive IQ Down-Conversion Subharmonic Mixer with Multiphase LO Distribution in 28 nm CMOS," in *2024 IEEE RFIC*, 2024, pp. 371–374.

[7] J. Zhang *et al.*, "A W-Band Spillover-Tolerant Mixer-First Receiver for FMCW Radars," in *2023 IEEE RFIC*, 2023, pp. 241–244.

[8] I. K. Aksoyak *et al.*, "A Highly Linear D -Band I/Q Receiver With Active Mixer-First Architecture in SiGe Technology," *IEEE TMTT*, 2024.

[9] H. Nam *et al.*, "A D-Band High-Linearity Down-Conversion Mixer for 6G Wireless Communications," *IEEE MWTL*, no. 5, pp. 579–582, 2023.